ACS APPLIED ELECTRONIC MATERIALS

pubs.acs.org/acsaelm

Article

Density Functional Analysis of Threshold Voltage Control by Oxide Dipole Layers in Si- and MoS_2-Based FETs

Ruyue Cao, Hailing Guo, Jun-Wei Luo, Yuzheng Guo, and John Robertson*

Cite This: ACS Appl. Electron. Mater. 2025, 7, 721−728

Read Online

ACCESS | Metrics & More | Article Recommendations | Supporting Information

ABSTRACT: The control of the threshold voltage V_{th} of high-k/metal metal-oxide-semiconductor field-effect transistor (MOSFET) gate stacks for n-type or p-type polarities by oxide dipole layers is analyzed by density functional theory. It is found that oxides such as SrO, Y_2O_3, HfO_2, Nb_2O_5 or amorphous Al_2O_3 could shift V_{th} to give either n- or p-polarities due to the band alignments and charge neutrality levels of the intrinsic virtual gap states of the oxides. This use of oxide layers for V_{th} control can be extended from Si MOSFETs to those using 2D transition metal dichalcogenide (TMD) channels such as MoS_2. The implementation of the dipole layer approach could allow bipolar operation of TMD-based FETs. As the presence of sulfur vacancies in MoS_2 can give their MOSFETs an extrinsic n-type character, we find that this doping effect could be compensated by an Al_2O_3 layer that shifts E_F downward toward midgap.

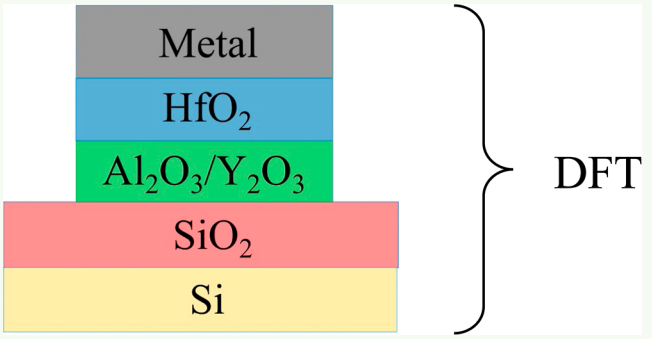

KEYWORDS: *density functional modeling, CMOS gate stacks, equivalent oxide thickness, 2D materials, Si, MoS_2, threshold voltage, charge neutrality level*

1. INTRODUCTION

One of the critical features of the operation of MOSFETs is to explain how to control the threshold voltage V_{th} of the n- and p-type devices, the primary parameter that sets their polarity. When SiO_2-based gate stacks on Si were first replaced by high-k dielectrics and metal gates, suitable gates for n- and p-type polarity devices were initially created by using two metals of different work functions.[1] These were then replaced by a single, midgap metal like TiN plus two dipole-shifting oxide layers to produce the n- and p-type MOSFETs,[2−8] as shown in Figure 1. This would then achieve n- and p-type inversion mode FETs. The use of two oxide "dipole layers" rather than n- and p-type gate metals was favored because it avoided having reactive n-type metal gates.

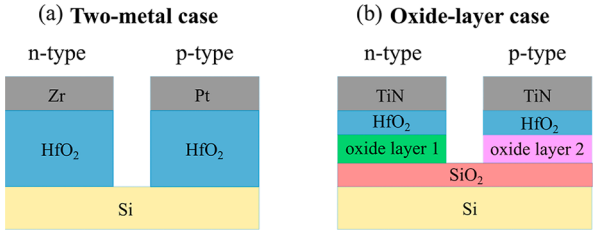

Figure 1. Comparison of different voltage threshold settings in MOS structures (a) two-metal case with n- and p-type metal gates to shift the gate voltage, (b) the oxide layer case with single TiN metal gate and an oxide layer to vary the gate voltage, V_{th}.

The dipole shift provided by such oxide layers was found to vary with the oxygen ion density in the gate dielectric in a semiempirical model proposed by Kita and Toriumi.[9] A recent *nonempirical* density functional theory (DFT) analysis suggested that the flat-band voltage shift of these oxide "dipole layers" could more fundamentally be based on their relative band alignments.[10] The present paper shows first that the effective electronegativity of the n- and p-gate oxide layers can be best expressed as the charge neutrality level (CNL) energy of the dipole layers, where the CNL represents the Fermi level of the evanescent metal-induced gap states (MIGS) of the oxides.[11] We then provide a simplified DFT description of the electronic structure of the entire gate stack and channel and the CNLs, starting with present-day Si channel semiconductors. This covers the industrially relevant SrO, Y_2O_3, HfO_2, Nb_2O_5 and amorphous Al_2O_3 gate dielectrics, to show how the present model using the CNL approach provides a more fundamental description. We then extend this from Si

Received: October 10, 2024
Revised: December 24, 2024
Accepted: December 25, 2024
Published: January 7, 2025

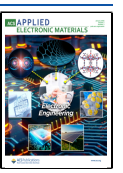

channels to possible future transition metal dichalcogenide (TMD) channel materials. This provides two alternative descriptions of the cause of the voltage shift in Figure 1b, in terms of dipole layers or charge neutrality levels, where the result can be chosen by which description gives the lowest total energy of the gate stack supercell.

Scaling will eventually require the replacement of Si channels by layered TMD semiconductors like MoS_2, as these theoretically outperform 3D semiconductors by retaining their carrier mobility down to very low channel thicknesses.[12] However, the thinness of TMDs makes them more susceptible to poor growth processes, extrinsic defects and electrical contact problems.[13−15] Nevertheless, optimized MoS_2 shows a direct or near-direct bandgap, a large on-current/off-current ratio ($I_{ON}/I_{OFF} > 10^8$), a low subthreshold slope and a reasonably high carrier mobility.[16] Recent advances include large-area few-layer MoS_2 deposited by chemical vapor deposition (CVD) and some progress toward viable manufacturing.[17−24] Thus, the paper extends our DFT analysis of V_{th} control of high-K gate stacks on Si to MOSFETs with MoS_2 channels. We finally treat MoS_2 channels containing some S vacancy defects which dope the MoS_2 n-type. Amorphous Al_2O_3 dipole layers are shown to able to compensate the n-type shift of S vacancies, allowing control of n-and p-FETs across the entire MoS_2 gap.

2. METHODS

We study the semiconductor channels and gate stacks by sizable atomic supercell models. Their atomic structures were relaxed by the CASTEP DFT code[25] employing ultrasoft pseudopotentials with a plane wave cutoff energy of 380 eV and the Perdew−Burke−Ernzerhof (PBE) version of generalized gradient approximation (GGA)[26] for the electronic exchange−correlation function and a 3 × 3 × 1 Monkhorst−Pack k-point grid for structural optimization. The energies are converged to 10^{-5} eV per atom and the forces are converged to 0.02 eV/Å. The electronic structure was then calculated for a denser k-point mesh of 5 × 5 × 1. Periodic images were prevented using a 15 Å thick vacuum layer between each supercell. Hybrid functionals[27] are used to correct the band gap in isolated nonmetallic parts of the supercell, but the GGA method is retained for gate stack supercells containing metallic gates otherwise these states will cause divergence. This need for convergence limits the overall supercell sizes. The DFT-D3 scheme Grimme et al.[28] was used to describe the weak van der Waals interactions between MoS_2 layers. A deeper description of their use in various situations is covered by Klimeš et al.[29]

The dipole layers could involve either crystalline or amorphous (a-) oxide phases. The monoclinic θ-Al_2O_3 polytype has a similar density and predominantly 4-fold Al sites[30,31] of a-Al_2O_3 rather than the more covalent, higher density and 6-fold Al site network of sapphire which has been used to represent atomic layer deposited Al_2O_3. Here though, a thin a-Al_2O_3 network was created by ab initio molecular dynamics (AIMD)[32] as follows. First, θ-Al_2O_3 was heated to 2500K for 9 ps with a time step of 3 fs to create a molten structure. After equilibration, the temperature was quenched back to room temperature for 10 ps for a cooling period of 2 fs. The supercell was then relaxed to its lowest-energy structure. For the calculation involving hexagonal MoS_2 we could use the relaxed θ-Al_2O_3 lattice.

The energy relaxation occurs relatively easily for the HfO_2 layers due to the facile diffusion of oxygen ions. However, the more covalent a-Al_2O_3 phase has a rigid network, which can become trapped in local energy minima. In that case, the a-Al_2O_3 layer and its interfaces are subjected to AIMD to surmount these energy barriers to find a global energy minimum. These are noted by comparing the total energies of the supercell (Figure S1 in the Supporting Information). It becomes evident that poorly converged solutions possess a combination of band alignment and dipole voltage shifts due to interfacial point defects. These eventually converge to a dominance of band alignment over voltage shifts at the global minimum. These simulations nevertheless use relatively thick oxide layers to show these differences, whereas ultrathin high-K oxide layers are needed technologically due to scaling.[33,34]

The V_{th} shift, E_F and band alignments in GGA are displayed by calculating the real-space layer by layer density of states (LDOS) plots using atomic layer slices of each supercell model. We use Ru rather than TiN in the calculations for simplicity as it has a similar work function to TiN.

The band alignments can also be visualized by a charge density versus energy versus distance plots using QuantumATK software.[35] An energy cutoff of 75 hartree and a 5 × 5 × 1 k-point grid was adopted. The Fermi−Dirac occupation was broadened by 1000 K to aid iteration convergence. The conduction band minimum of Al_2O_3 appears at higher than expected energies in the ATK plots because of their low DOS compared to those of the O 2p or metal d bands.

3. RESULTS

3.1. Role of Charge Neutrality Level. The key interface of the gate stack is that between gate electrode and the oxide dielectric layer (treated as a wide-gap semiconductor). The band alignment at this interface depends on any charge transfer at the interface between the metal states and the dielectric in terms of the extent of evanescent interface states into the dielectric layer and their resulting dipole moment.[11] The Schottky barrier height (SBH) for electrons ϕ_n between a semiconductor S and a metal M is given by[36,37]

$$\phi_n = S(\Phi_M - \Phi_S) + (\Phi_S - \chi_s) \quad (1)$$

where Φ_M is the work function of the metal, Φ_S is the energy of the semiconductor interface states, χ_S is the semiconductor's electron affinity (EA) and S is the Schottky pinning parameter. S is given by[38]

$$S = \frac{1}{1 + \frac{e^2 N\delta}{\varepsilon\varepsilon_0}} \quad (2)$$

where e is the electronic charge, ε_0 is the permittivity of free space, N is the areal density of the interface states and δ is their decay length into the dielectric/semiconductor layer. The dimensionless pinning factor S describes if the barrier is "pinned" or not. S varies between the limits $S = 1$ for unpinned Schottky barriers to $S = 0$ for barriers pinned by a high density of gap states. We assume that this interface is dominated by intrinsic metal-induced gap states (MIGS) not defects. Empirically, Mönch[39,40] found empirically that S varied with ε_∞ as

$$S = \frac{1}{1 + 0.1(\varepsilon_\infty - 1)^2} \quad (3)$$

here, the dielectric consists of an HfO_2 layer plus the dipole shifting layer gives a combined ε_∞ value in this case. The ε_∞ of the oxides are listed in Table 2, their typical S value is 0.6.

We first studied the band-edge energies for isolated bulk oxide slabs using hybrid functionals, including rock-salt SrO, fluorite HfO_2, hexagonal Y_2O_3, hexagonal La_2O_3 (ref 41), a Nb_2O_5 phase[42] and monoclinic θ-Al_2O_3.[31,42,43] These oxides each have a band gap of ∼6 eV and are chosen for industrial relevance at the time. Each bulk slab has 10 oxide layers terminated by a nonpolar (001) face bounded by 15 Å of vacuum, where the number of layers is defined by the number of cation layers. The surface layer possesses half the oxygen ion density of the bulk to ensure charge neutrality. The band-edge

https://doi.org/10.1021/acsaelm.4c01790
ACS Appl. Electron. Mater. 2025, 7, 721−728

Table 1. List of the Crystal Structure, Surface Cleavage Plane, and Rotation Angle of Each Material Shown in Figures 3a,b and 4a,b

	Figure 3a	Figure 3b	Figure 4a	Figure 4d
Si	cubic (001)	cubic (001)		
	45°	45°		
SiO_2	β-cristobalite (001)	β-cristobalite (001)		
	0°	0°		
Al_2O_3	monoclinic θ (100)			monoclinic θ (100)
	45°			45°
Y_2O_3		cubic (001)		
		0°		
HfO_2	fluorite (001)	fluorite (001)	fluorite (111)	fluorite (111)
	45°	45°	0°	30°
Ru	cubic (001)	cubic (001)	cubic (111)	cubic (111)
	0°	0°	0°	0°
MoS_2			hexagonal (001)	hexagonal (001)
			0°	30°

Table 2. Electronic Component of Dielectric Constant ε_∞ of Various Oxide Layers for Figure 2

material	ε_∞
HfO_2	3.61
SrO	3.28
La_2O_3	3.78
Y_2O_3	3.72
Nb_2O_5	5.48
a-Al_2O_3	1.71

energies of each oxide are calculated with respect to the vacuum level of the supercell by HSE to find their electron affinities (EA) and ionization potentials (IP). The band alignments of these oxides are seen in Figure 2a where the energy bands of SrO are seen to lie closest to the vacuum, followed by La_2O_3, Y_2O_3, HfO_2, Nb_2O_5 and last θ-Al_2O_3. Y_2O_3 is preferred to La_2O_3 in supercell calculations because it has a closer lattice matching to other oxide layers. The opposing electronegativity of Y_2O_3 and Al_2O_3 compared to HfO_2 allows this system to define the swing between n- and p-type FET polarities and their effective gate work functions. The CNL of Y_2O_3 was calculated as normal. However, the conduction band of La_2O_3 unlike Y_2O_3 contains highly localized empty 4d states which barely affect the CNL calculation.[41] Thus, there, we replace the La_2O_3 cell by a Y_2O_3 cell with no 4d states and its lattice constants dilated to that of La_2O_3 for the CNL calculation.

The CNL is the branch point of the semiconductor interface states, so it is the integral of the Greens function of the band structure within a certain energy range taken over the Brillouin zone,[36,37]

$$G(E) = \int_{BZ} \frac{N(E')\mathrm{d}'E}{E - E'} = 0 \tag{4}$$

This can be replaced by summing over bands and special points of the Brillouin zone[44]

$$G(E) = \sum_i \frac{1}{E - E_i} \tag{5}$$

Given the inverse relationship of G to E_i, large numbers of anion VB states repel the CNL upward and large numbers of CB cation states repel it downward.[37] Here, the short expression for E_{CNL} is used, with $E_{CNL} = (N_1E_2 + N_2E_1)/(N_1 + N_2)$ with 1 = vb, 2 = cb. The integral extends in energy from the bottom of the O 2p band to the top of the 4d or 5d states in the conduction band, or to an equivalent number of bands to match the charge transfer in Al_2O_3. States of higher energy are considered to be too delocalized to matter. Some of the CNL values are updated from earlier tabulations.[43] The calculated CNL and band extrema energies of the series SrO, La_2O_3, Y_2O_3, HfO_2, amorphous Al_2O_3 and Nb_2O_5 are shown in Figure 2a. The FET gate voltages $E_{n,p}$ are given as the sum of the Fermi energy of the common gate (E_g), plus the CNL difference between the n or p oxide shifting layers (a,b)

$$E_{n,p} = E_g + S(E_{CNL,a} - E_{CNL,b}) \tag{6}$$

where S is the Fermi level pinning factor. Figure 2b compares the calculated CNLs to the experimental flat band voltages as found by Kita and Toriumi[9] and others.[4,5,7] There is a surprisingly good linear fit. This fit gives S close to S = 0.47 using eq 6 and compares with S = 0.55 from ε_∞ ~3.6 of Table 2.

A previous analysis in terms of dopant band calculations found that it was difficult to extend dipole layers to more

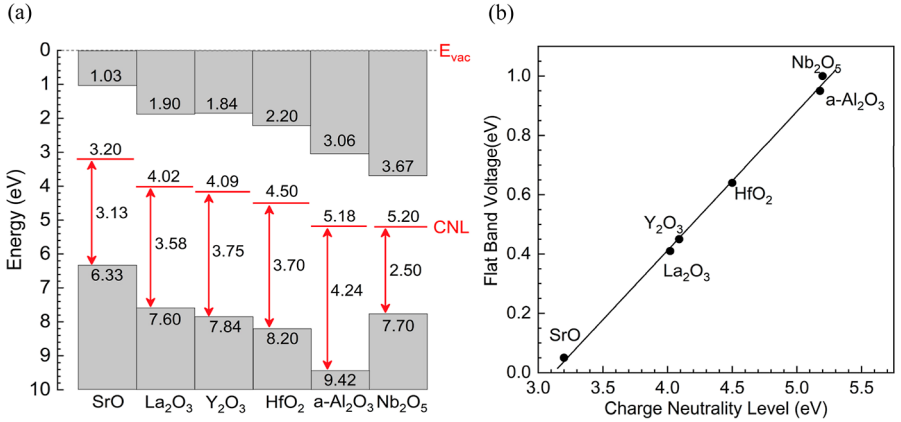

Figure 2. (a) Band alignments and charge neutrality levels of the six oxides considered here. E_{vac} is the vacuum level. (b) Experimental flat band voltage V_{th} vs calculated charge neutrality level (CNL) energy.

https://doi.org/10.1021/acsaelm.4c01790
ACS Appl. Electron. Mater. 2025, 7, 721−728

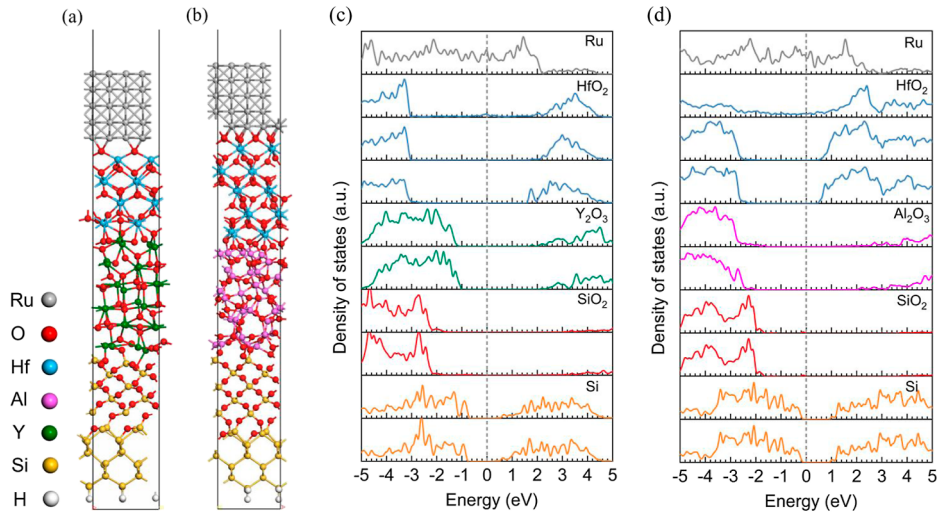

Figure 3. Relaxed structures and the corresponding LDOS of (a,c) $Si/SiO_2/Y_2O_3/HfO_2/Ru$ and (b,d) $Si/SiO_2/a\text{-}Al_2O_3/HfO_2/Ru$ gate stack supercells.

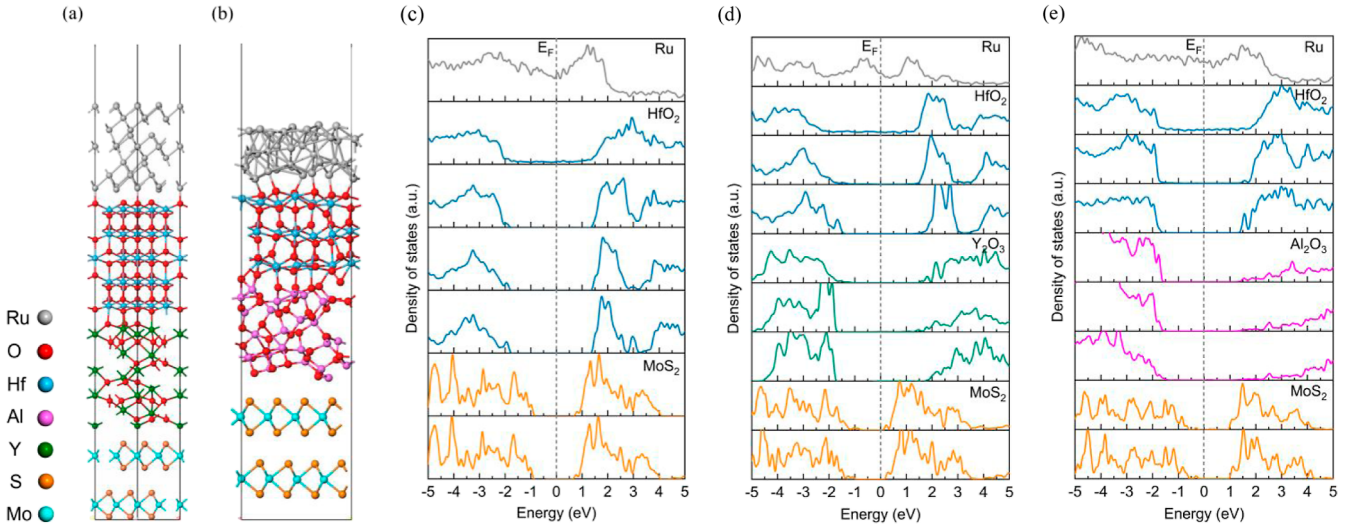

Figure 4. Relaxed structures of (a) $MoS_2/Y_2O_3/HfO_2/Ru$ and (b) $MoS_2/a\text{-}Al_2O_3/HfO_2/Ru$ gate stacks and LDOS of (c) $MoS_2/HfO_2/Ru$, (d) $MoS_2/HfO_2/Y_2O_3/Ru$ and (e) $MoS_2/a\text{-}Al_2O_3/HfO_2/Ru$ gate stack supercells, showing the change in offset voltages with respect to E_F in the LDOS (d,e).

electronegative oxides that Al_2O_3. On the other hand, it is clear that the CNL energy of SrO is much more electropositive than La_2O_3 if this biasing method is needed for wider gap channel semiconductors.

3.2. Supercell Calculations. Figure 3a,b shows relaxed atomic supercell models of $Si/SiO_2/Y_2O_3/HfO_2/Ru$ and $Si/SiO_2/a\text{-}Al_2O_3/HfO_2/Ru$ gate stacks which have a total cell size of 206 atoms. The supercells are seen to be asymmetric. As there is no overall current flow, there is no net voltage across each cell. The lateral cell size is chosen to minimize the lattice mismatch without costing unnecessary computational time. During this relaxation, we fixed the interfacial in-plane cell size to that of Si, because these various materials are grown on Si substrates, which have a lattice parameter of 5.43 Å after GGA relaxation.

Table 1 shows the details of the crystal structures, surface cleavage plane, and rotation angle of these lattices. The Si and HfO_2 lattices are rotated by 45°, while the SiO_2 and Ru lattices are not rotated. For the $Si/SiO_2/Al_2O_3/HfO_2/Ru$ cell, the θ-Al_2O_3 lattice is rotated by 45° and then subjected to AIMD, while Y_2O_3 is rotated by 30° and relaxed for the $Si/SiO_2/Y_2O_3/HfO_2/Ru$ supercell.

Figure 3c,d shows the GGA layered DOS (LDOS) with Y_2O_3 and a-Al_2O_3 shifting layers and other layers in the gate stacks on Si. Inserting the Y_2O_3 layer between SiO_2 and HfO_2 causes an effective upward shift of E_F toward the Si CBM, showing weak n-type behavior in this cell. This behavior is also in good agreement with the ATK LDOS diagram to be shown later. Insertion of an Al_2O_3 layer between SiO_2 and HfO_2 in Figure 3d shifts E_F toward the VBM of Si and p-type behavior. The voltage shifts of E_F between n- and p-type dipole layers from the LDOS can be seen from the 0.6 eV E_F shift, using the Ru 4d core levels as reference. This method allows a more precise estimate of E_F shift than the LDOS plots themselves. This shows that the dipole layer method is controlling the E_F polarity. La_2O_3 could provide a slightly larger shift. Note that in this model, the effect of any SiO_2 layer is termed extrinsic and its role is not covered.

https://doi.org/10.1021/acsaelm.4c01790
ACS Appl. Electron. Mater. 2025, 7, 721−728

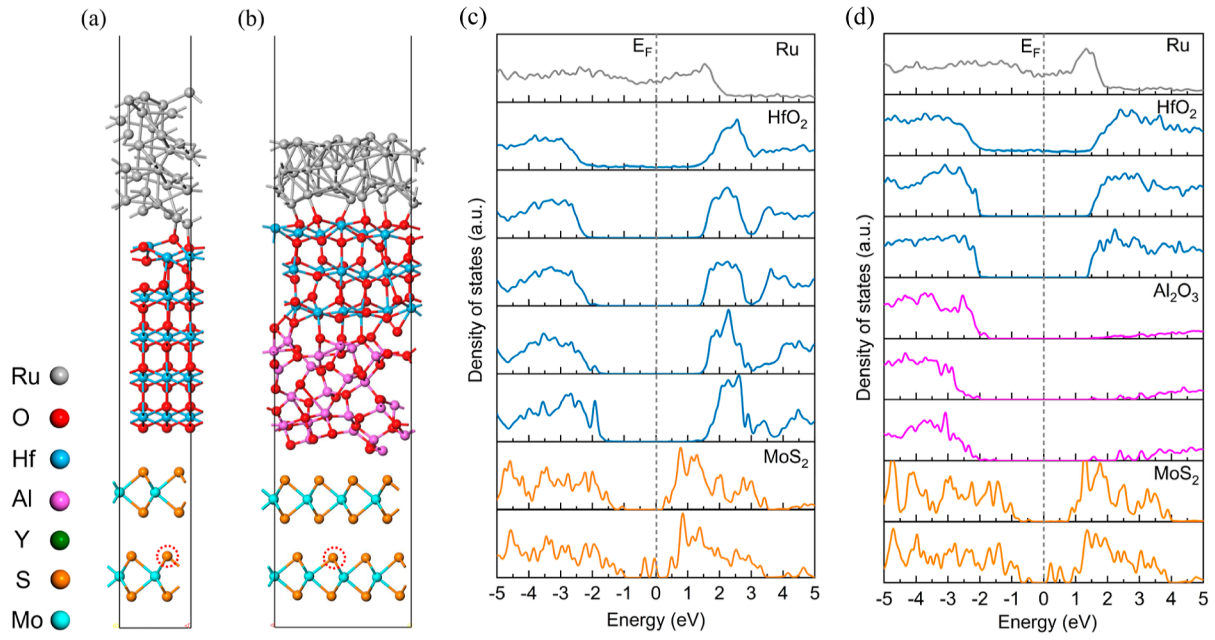

Figure 5. Relaxed structures and LDOSs of (a,c) MoS_2 with S vacancy and (b,d) MoS_2 with S vacancy and Al_2O_3 dipole shifting layers. Note the near midgap states due to S vacancy.

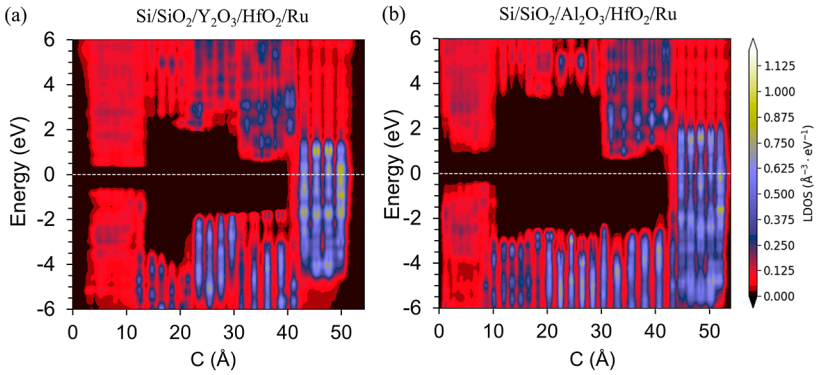

Figure 6. Plot of LDOS band images vs energy scales for (a) Y_2O_3 and (b) a-Al_2O_3 dipole shifting layers for Si high-K gate stack supercells.

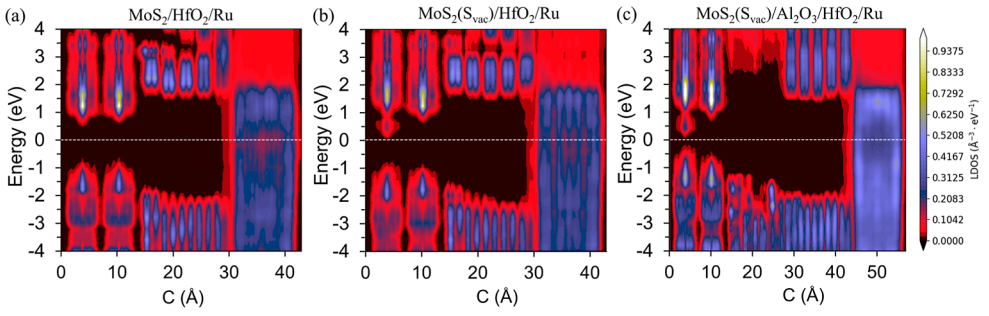

Figure 7. Plot of LDOS images vs energy scales for (a) defect-free MoS_2 and (b) MoS_2 with S vacancy and (c) MoS_2/a-Al_2O_3/HfO_2/Ru with S vacancy.

We can then examine the effect of dipole layers in controlling V_{th} shifts for MoS_2 channel layers. We use Ru/HfO_2/MoS_2 cells with either Y_2O_3 or a-Al_2O_3 layers inserted between the HfO_2 layer and the MoS_2 using the supercells shown in Figure 4a,b. There are no primary bonds between the oxides and the MoS_2. The CNLs of the dipole layers are given in Figure 2. The MoS_2/Y_2O_3/HfO_2/Ru supercell of 273 atoms is constructed by cleaving HfO_2 along (111) and then rotating it by 30°, while the Y_2O_3 lattice is rotated by 45°. For the MoS_2/Al_2O_3/HfO_2/Ru cell, HfO_2 is cleaved along (111) and then rotated by 30°, while the θ-Al_2O_3 lattice is rotated by 45°. Ru is also cleaved along (111) for both MoS_2-based interface models. Ru is also cleaved along (111) for both MoS_2-based interface models.

To capture the layered characteristics of each model, the layer density of states (LDOS) for the three fully relaxed

https://doi.org/10.1021/acsaelm.4c01790
ACS Appl. Electron. Mater. 2025, 7, 721−728

MoS_2-related supercells are calculated. Figure 4c−e shows that there are no gap states caused by interfacial defects present at either Ru/HfO_2, HfO_2/MoS_2, HfO_2/Al_2O_3, Y_2O_3/MoS_2 or Al_2O_3/MoS_2 interfaces. Thus, these should not cause potentials that affect the V_{th}. Also, any MIGS from the gate electrode only appear for the early layers of HfO_2 and decay rapidly to zero at the second layer, implying a well-defined structure. The layered density of states in Figures 4 and 5 are in good agreement with the LDOSs in shown later in Figure 7, that the emergence of Al_2O_3 to the insulator causes the downward E_F shift, approaching the VBM of MoS_2. The VBM band edge of Al_2O_3 exhibits a slope, indicating the presence of a small remaining electric field within Al_2O_3. This suggests that dipoles can control the movement of the E_F across the entire band gap, allowing, in principle, a full range of bipolar FET behavior in the wider gap of MoS_2.

We now consider the effect of extrinsic defects in MoS_2. The presence of sulfur vacancies S_{vac} in MoS_2 causes it to become extrinsic n-type.[33] The vacancy is not chemically passivated by hydrogen,[45−47] unlike P_b centers in Si, owing to the absence of 2-electron bonds in the MoS_2 lattice. Lien et al.[48] were able to restore the photoluminescence (PL) signal of MoS_2 by electrically quenching its photoexcited trions, yet the underlying defect states remained chemically unpassivated. Thus, Pop et al.[21,33,34,49,50] noted that these TMD devices had not yet achieved true inversion-mode FETs, primarily due to the unpassivated defect states of S_{vac}. Thus, incorporating a V_{th} shifting layer might allow full inversion of these FETs.

We therefore constructed a S_{vac} defect at the MoS_2 layer away from the HfO_2 layer in the supercell shown in Figure 5a. The LDOS in Figure 5b shows the appearance of vacancy defect states near the CBM of the first layer of MoS_2, shifting E_F upward, giving the system n-type conductivity. We then introduced an a-Al_2O_3 layer between MoS_2 and HfO_2. We see in Figure 5d that the Al_2O_3 layer lowers E_F toward the VBM, giving p-type behavior. This result confirms that dipole layer can control the threshold voltage.

It is also useful to extend this GGA supercell analysis to display the results using local orbital QuantumATK imaging, as in Figure 6 and 7. This displays the partial density of states of each layer of the supercell as a color-coded map of the LDOS showing the band edges vs ethe energy axis vs the layers across the supercell so than the effects of field gradients can be seen. Note that the conduction band minimum of Al_2O_3 appears at higher than expected energies in the ATK plots (Figures 6, 7) because of their low density of states compared to the O 2p or metal d bands.

Figure 6a,b compares the supercell with the n-type Y_2O_3 dipole-shifting layer to the p-type a-Al_2O_3 shifting layer acting on a gate stack with an Si channel. E_F at the Ru metal has a fixed energy. The high CBM of the Y_2O_3 layer is clearly seen in Figure 6a,b shows the E_F lying at lower energies near the VBM in the p-type case. The supercell has mainly band alignment shifts and only small electric fields within the layers, except for the SiO_2 layer. The Al_2O_3 oxide layer has a smaller CB density of states due to its s-like character, much lower than the O 2p character of the upper VB band, so its CBM is not fully displayed in the LDOS plots. There is a field across the HfO_2 layer in this case.

The effect of the S vacancy and its passivation is displayed in Figure 7. Figure 7a shows the color plot of the density of states and the energy level of undoped gate stack with MoS_2 channel with HfO_2 gate stack/Ru. Figure 7b shows this with a S vacancy in one of the MoS_2 channel sites, with E_F moving closer to the CBM. Figure 7c shows the effect of the Al_2O_3 dipole-shifting layer. The defect level in the MoS_2 channel has been passivated, in that the S vacancy is now positively charged and its states are now unoccupied. E_F now lies near midgap again, consistent with Figure 5.

We have introduced a fully density functional model of gate stacks. In order to distinguish between dipole layer model and one involving band offsets to the component oxides it was necessary to use thick oxide layers. In practice ultrathin oxide must now be used in order to keep up with dimensional scaling, as found for example in recent work of Pop et al.[34,49,50]

4. CONCLUSIONS

We develop a theory of bipolar gate stacks consisting of a single midgap metal with two different oxides to set each gate polarities. The oxide electronegativity is shown to be given by the oxide charge neutrality level energies, a measurable quantity rather than empirically related to the oxide ion areal density, so the overall gate voltage shift depends on the CNL energy difference of the oxides. This is found to describe well the experimentally observed flat band voltage shift of the gate stacks. In general, dipole voltage shifts and CNL energy differences both contribute to flat band voltage differences, but the CNL band alignments tend to have the lowest total energy. This model is then supported by a more detailed density functional theory analysis of the overall flat band voltage shifts in oxide gate stacks. This allows further development in terms of the addition of extrinsic defect centers and to much lower effective oxide thickness.

■ ASSOCIATED CONTENT

Data Availability Statement

The data supporting this study's findings are available from the corresponding author upon reasonable request.

Supporting Information

The Supporting Information is available free of charge at https://pubs.acs.org/doi/10.1021/acsaelm.4c01790.

Showing the optimization of the total energy of the MoS_2 with S vacancy supercell and its passivation (PDF)

■ AUTHOR INFORMATION

Corresponding Author

John Robertson − *Engineering Department, Cambridge University, Cambridge CB2 1PZ, U.K.; Electrical Engineering and Automation, Wuhan University, Wuhan 430042, China;* orcid.org/0000-0001-6558-528X; Email: jr214@cam.ac.uk

Authors

Ruyue Cao − *Engineering Department, Cambridge University, Cambridge CB2 1PZ, U.K.; State Key Laboratory of Superlattices and Microstructures, Institute of Semiconductors, Chinese Academy of Sciences, Beijing 100083, China;* orcid.org/0000-0003-2678-6710

Hailing Guo − *Electrical Engineering and Automation, Wuhan University, Wuhan 430042, China*

Jun-Wei Luo − *State Key Laboratory of Superlattices and Microstructures, Institute of Semiconductors, Chinese Academy of Sciences, Beijing 100083, China;* orcid.org/0000-0002-1147-8267

https://doi.org/10.1021/acsaelm.4c01790
ACS Appl. Electron. Mater. 2025, 7, 721−728

Yuzheng Guo − *Electrical Engineering and Automation, Wuhan University, Wuhan 430042, China;* orcid.org/0000-0001-9224-3816

Complete contact information is available at: https://pubs.acs.org/10.1021/acsaelm.4c01790

Notes

The authors declare no competing financial interest.

■ ACKNOWLEDGMENTS

This work was supported by the CAS Project for Young Scientists in Basic Research under Grant no. YSBR-026, and Open Fund of Hubei Key Laboratory of Electronic Manufacturing and Packaging Integration (Wuhan University) (Grant no. EMPI2024008). The numerical calculations used the HPC in the University of Cambridge and the Supercomputing Center of Wuhan University.

■ REFERENCES

(1) Chau, R.; Datta, S.; Doczy, M.; Doyle, B.; Kavalieros, J.; Metz, M. High-k/Metal−Gate Stack and Its MOSFET Characteristics. *IEEE Electron Device Lett.* **2004**, *25*, 408−410.

(2) Iwamoto, K.; Kamimuta, Y.; Ogawa, A.; Watanabe, Y.; Migita, S.; Mizubayashi, W.; Morita, Y.; Takahashi, M.; Ota, H.; Nabatame, T.; Toriumi, A. Experimental Evidence for the Flatband Voltage Shift of High-k Metal-Oxide-Semiconductor Devices Due to the Dipole Formation at the High-k/SiO2 Interface. *Appl. Phys. Lett.* **2008**, *92*, 132907.

(3) Yamamoto, Y.; Kita, K.; Kyuno, K.; Toriumi, A. Study of La-Induced Flat Band Voltage Shift in Metal/HfLaO $_x$/SiO $_2$/Si Capacitors. *Jpn. J. Appl. Phys.* **2007**, *46*, 7251.

(4) Guha, S.; Paruchuri, V. K.; Copel, M.; Narayanan, V.; Wang, Y. Y.; Batson, P. E.; Bojarczuk, N. A.; Linder, B.; Doris, B. Examination of Flatband and Threshold Voltage Tuning of HfO2/TiN Field Effect Transistors by Dielectric Cap Layers. *Appl. Phys. Lett.* **2007**, *90*, 092902.

(5) Kirsch, P. D.; Sivasubramani, P.; Huang, J.; Young, C. D.; Quevedo-Lopez, M. A.; Wen, H. C.; Alshareef, H.; Choi, K.; Park, C. S.; Freeman, K.; Hussain, M. M.; Bersuker, G.; Harris, H. R.; Majhi, P.; Choi, R.; Lysaght, P.; Lee, B. H.; Tseng, H.-H.; Jammy, R.; Böscke, T. S.; Lichtenwalner, D. J.; Jur, J. S.; Kingon, A. I. Dipole Model Explaining High-k/Metal Gate Field Effect Transistor Threshold Voltage Tuning. *Appl. Phys. Lett.* **2008**, *92*, 092901.

(6) Lee, B. H.; Oh, J.; Tseng, H. H.; Jammy, R.; Huff, H. Gate Stack Technology for Nanoscale Devices. *Mater. Today* **2006**, *9*, 32−40.

(7) Linder, B.; Narayanan, V.; Paruchuri, V. K.; Cartier, E.; Kanakasabapathy, S. Gate First PFET Poly-Si/TiN/Al2O3 Gate Stacks with Inversion Thicknesses Less than 15Å for High Performance or Low Power CMOS Applications *2007 International Conference on Solid State Devices and Materials*; Tsukuba International Congress Center: Ibaraki, Japan, 2007.

(8) Coss, B. E.; Loh, W.-Y.; Wallace, R. M.; Kim, J.; Majhi, P.; Jammy, R. Near Band Edge Schottky Barrier Height Modulation Using High-κ Dielectric Dipole Tuning Mechanism. *Appl. Phys. Lett.* **2009**, *95*, 222105.

(9) Kita, K.; Toriumi, A. Origin of Electric Dipoles Formed at High-k/SiO2 Interface. *Appl. Phys. Lett.* **2009**, *94*, 132902.

(10) Cao, R.; Zhang, Z.; Guo, Y.; Robertson, J. Density Functional Analysis of Oxide Dipole Layer Voltage Shifts in High κ/Metal Gate Stacks. *J. Appl. Phys.* **2023**, *134*, 085302.

(11) Tersoff, J. Schottky Barrier Heights and the Continuum of Gap States. *Phys. Rev. Lett.* **1984**, *52*, 465−468.

(12) Akinwande, D.; Huyghebaert, C.; Wang, C.-H.; Serna, M. I.; Goossens, S.; Li, L.-J.; Wong, H.-S. P.; Koppens, F. H. L. Graphene and Two-Dimensional Materials for Silicon Technology. *Nature* **2019**, *573*, 507−518.

(13) Guo, Y.; Liu, D.; Robertson, J. Chalcogen Vacancies in Monolayer Transition Metal Dichalcogenides and Fermi Level Pinning at Contacts. *Appl. Phys. Lett.* **2015**, *106*, 173106.

(14) Das, S.; Chen, H.-Y.; Penumatcha, A. V.; Appenzeller, J. High Performance Multilayer MoS $_2$ Transistors with Scandium Contacts. *Nano Lett.* **2013**, *13*, 100−105.

(15) Gong, C.; Colombo, L.; Wallace, R. M.; Cho, K. The Unusual Mechanism of Partial Fermi Level Pinning at Metal−MoS$_2$ Interfaces. *Nano Lett.* **2014**, *14*, 1714−1720.

(16) Yoon, Y.; Ganapathi, K.; Salahuddin, S. How Good Can Monolayer MoS $_2$ Transistors Be? *Nano Lett.* **2011**, *11*, 3768−3773.

(17) Choudhury, T. H.; Zhang, X.; Al Balushi, Z. Y.; Chubarov, M.; Redwing, J. M. Epitaxial Growth of Two-Dimensional Layered Transition Metal Dichalcogenides. *Annu. Rev. Mater. Res.* **2020**, *50*, 155−177.

(18) Zhu, J.; Park, J.-H.; Vitale, S. A.; Ge, W.; Jung, G. S.; Wang, J.; Mohamed, M.; Zhang, T.; Ashok, M.; Xue, M.; Zheng, X.; Wang, Z.; Hansryd, J.; Chandrakasan, A. P.; Kong, J.; Palacios, T. Low-Thermal-Budget Synthesis of Monolayer Molybdenum Disulfide for Silicon Back-End-of-Line Integration on a 200 Mm Platform. *Nat. Nanotechnol.* **2023**, *18*, 456−463.

(19) Si, M.; Su, C.-J.; Jiang, C.; Conrad, N. J.; Zhou, H.; Maize, K. D.; Qiu, G.; Wu, C.-T.; Shakouri, A.; Alam, M. A.; Ye, P. D. Steep-Slope Hysteresis-Free Negative Capacitance MoS2 Transistors. *Nat. Nanotechnol.* **2018**, *13*, 24−28.

(20) Schram, T.; Sutar, S.; Radu, I.; Asselberghs, I. Challenges of Wafer-Scale Integration of 2D Semiconductors for High-Performance Transistor Circuits. *Adv. Mater.* **2022**, *34*, 2109796.

(21) English, C. D.; Shine, G.; Dorgan, V. E.; Saraswat, K. C.; Pop, E. Improved Contacts to MoS $_2$ Transistors by Ultra-High Vacuum Metal Deposition. *Nano Lett.* **2016**, *16*, 3824−3830.

(22) Wang, X.; Kim, S. Y.; Wallace, R. M. Interface Chemistry and Band Alignment Study of Ni and Ag Contacts on MoS $_2$. *ACS Appl. Mater. Interfaces* **2021**, *13*, 15802−15810.

(23) Wang, Y.; Kim, J. C.; Wu, R. J.; Martinez, J.; Song, X.; Yang, J.; Zhao, F.; Mkhoyan, A.; Jeong, H. Y.; Chhowalla, M. Van Der Waals Contacts between Three-Dimensional Metals and Two-Dimensional Semiconductors. *Nature* **2019**, *568*, 70−74.

(24) Zhang, Z.; Guo, Y.; Robertson, J. Reduced Fermi Level Pinning at Physisorptive Sites of Moire-MoS $_2$/Metal Schottky Barriers. *ACS Appl. Mater. Interfaces* **2022**, *14*, 11903−11909.

(25) Clark, S. J.; Segall, M. D.; Pickard, C. J.; Hasnip, P. J.; Probert, M. I. J.; Refson, K.; Payne, M. C. First Principles Methods Using CASTEP. *Z. Für Krist. - Cryst. Mater.* **2005**, *220*, 567−570.

(26) Perdew, J. P.; Burke, K.; Ernzerhof, M. Generalized Gradient Approximation Made Simple. *Phys. Rev. Lett.* **1996**, *77*, 3865−3868.

(27) Heyd, J.; Scuseria, G. E.; Ernzerhof, M. Hybrid Functionals Based on a Screened Coulomb Potential. *J. Chem. Phys.* **2003**, *118*, 8207−8215.

(28) Grimme, S.; Antony, J.; Ehrlich, S.; Krieg, H. A Consistent and Accurate *Ab Initio* Parametrization of Density Functional Dispersion Correction (DFT-D) for the 94 Elements H-Pu. *J. Chem. Phys.* **2010**, *132*, 154104.

(29) Klimeš, J.; Bowler, D. R.; Michaelides, A. Van Der Waals Density Functionals Applied to Solids. *Phys. Rev. B* **2011**, *83*, 195131.

(30) Afanas'ev, V. V.; Stesmans, A. Internal Photoemission at Interfaces of High-κ Insulators with Semiconductors and Metals. *J. Appl. Phys.* **2007**, *102*, 081301.

(31) Liu, D.; Clark, S. J.; Robertson, J. Oxygen Vacancy Levels and Electron Transport in Al2O3. *Appl. Phys. Lett.* **2010**, *96*, 032905.

(32) Car, R.; Parrinello, M. Unified Approach for Molecular Dynamics and Density-Functional Theory. *Phys. Rev. Lett.* **1985**, *55*, 2471−2474.

(33) English, C. D.; Smithe, K. K. H.; Xu, R. L.; Pop, E. Approaching Ballistic Transport in Monolayer MoS2 Transistors with Self-Aligned 10 Nm Top Gates *2016 IEEE International Electron Devices Meeting (IEDM)*; IEEE: San Francisco, CA, USA, 2016, pp 5 6 1−5 6 4.

(34) Ko, J.-S.; Shearer, A.; Lee, S.; Neilson, K.; Jaikissoon, M.; Kim, K.; Bent, S.; Saraswat, K. C.; Pop, E. Achieving 1-Nm-Scale

Equivalent Oxide Thickness Top Gate Dielectric on Monolayer Transition Metal Dichalcogenide Transistors with CMOS-Friendly Approaches *Proc. 2024 IEEE Symposium on VLSI Technology & Circuits*; IEEE, 2024.
(35) Smidstrup, S.; Markussen, T.; Vancraeyveld, P.; Wellendorff, J.; Schneider, J.; Gunst, T.; Verstichel, B.; Stradi, D.; Khomyakov, P. A.; Vej-Hansen, U. G.; Lee, M.-E.; Chill, S. T.; Rasmussen, F.; Penazzi, G.; Corsetti, F.; Ojanperä, A.; Jensen, K.; Palsgaard, M. L. N.; Martinez, U.; Blom, A.; Brandbyge, M.; Stokbro, K. QuantumATK: An Integrated Platform of Electronic and Atomic-Scale Modelling Tools. *J. Phys.: Condens. Matter* **2020**, *32*, 015901.
(36) Robertson, J. Band Offsets of Wide-Band-Gap Oxides and Implications for Future Electronic Devices. *J. Vac. Sci. Technol., B: Microelectron. Nanometer Struct.–Process., Meas., Phenom.* **2000**, *18*, 1785−1791.
(37) Robertson, J. Band Structures and Band Offsets of High K Dielectrics on Si. *Appl. Surf. Sci.* **2002**, *190*, 2−10.
(38) Cowley, A. M.; Sze, S. M. Surface States and Barrier Height of Metal-Semiconductor Systems. *J. Appl. Phys.* **1965**, *36*, 3212−3220.
(39) Mönch, W. Role of Virtual Gap States and Defects in Metal-Semiconductor Contacts. *Phys. Rev. Lett.* **1987**, *58*, 1260−1263.
(40) Mönch, W. Chemical Trends of Barrier Heights in Metal-Semiconductor Contacts: On the Theory of the Slope Parameter. *Appl. Surf. Sci.* **1996**, *92*, 367−371.
(41) Gillen, R.; Clark, S. J.; Robertson, J. Nature of the Electronic Band Gap in Lanthanide Oxides. *Phys. Rev. B* **2013**, *87*, 125116.
(42) Sathasivam, S.; Williamson, B. A. D.; Althabaiti, S. A.; Obaid, A. Y.; Basahel, S. N.; Mokhtar, M.; Scanlon, D. O.; Carmalt, C. J.; Parkin, I. P. Chemical Vapor Deposition Synthesis and Optical Properties of Nb_2O_5 Thin Films with Hybrid Functional Theoretical Insight into the Band Structure and Band Gaps. *ACS Appl. Mater. Interfaces* **2017**, *9*, 18031−18038.
(43) Robertson, J. Band Offsets, Schottky Barrier Heights, and Their Effects on Electronic Devices. *J. Vac. Sci. Technol., A* **2013**, *31*, 050821.
(44) Cardona, M.; Christensen, N. E. Acoustic Deformation Potentials and Heterostructure Band Offsets in Semiconductors. *Phys. Rev. B* **1987**, *35*, 6182−6194.
(45) Amani, M.; Lien, D.-H.; Kiriya, D.; Xiao, J.; Azcatl, A.; Noh, J.; Madhvapathy, S. R.; Addou, R.; Kc, S.; Dubey, M.; Cho, K.; Wallace, R. M.; Lee, S.-C.; He, J.-H.; Ager, J. W.; Zhang, X.; Yablonovitch, E.; Javey, A. Near-Unity Photoluminescence Quantum Yield in MoS_2. *Science* **2015**, *350*, 1065−1068.
(46) Lu, H.; Kummel, A.; Robertson, J. Passivating the Sulfur Vacancy in Monolayer MoS2. *APL Mater.* **2018**, *6*, 066104.
(47) Ahn, B.; Kim, Y.; Kim, M.; Yu, H. M.; Ahn, J.; Sim, E.; Ji, H.; Gul, H. Z.; Kim, K. S.; Ihm, K.; Lee, H.; Kim, E. K.; Lim, S. C. One-Step Passivation of Both Sulfur Vacancies and SiO_2 Interface Traps of MoS_2 Device. *Nano Lett.* **2023**, *23*, 7927−7933.
(48) Lien, D.-H.; Uddin, S. Z.; Yeh, M.; Amani, M.; Kim, H.; Ager, J. W.; Yablonovitch, E.; Javey, A. Electrical Suppression of All Nonradiative Recombination Pathways in Monolayer Semiconductors. *Science* **2019**, *364*, 468−471.
(49) McClellan, C. J.; Yalon, E.; Smithe, K. K. H.; Suryavanshi, S. V.; Pop, E. High Current Density in Monolayer MoS_2 Doped by AlO_x. *ACS Nano* **2021**, *15*, 1587−1596.
(50) Ko, J.-S.; Lee, S.; Bennett, R. K. A.; Schauble, K.; Jaikisson, M.; Neilson, K.; Kim, K.; Saraswat, K.; Pop, E. Nanoletts. **2024** accepted.

https://doi.org/10.1021/acsaelm.4c01790
ACS Appl. Electron. Mater. 2025, 7, 721−728